CHALMERS
UNIVERSITY OF TECHNOLOGY

Alignment of Multi-Frequency SAR Images Acquired over Sea Ice Using Drift Compensation

Citation for the original published paper (version of record):
Demchev, D., Eriksson, L., Hildeman, A. et al (2023). Alignment of Multi-Frequency SAR Images Acquired over Sea Ice Using Drift Compensation. IEEE Journal of Selected Topics in Applied Earth Observations and Remote Sensing, 16: 7393-7402. http://dx.doi.org/10.1109/JSTARS.2023.3302576

(article starts on next page)

Alignment of Multifrequency SAR Images Acquired Over Sea Ice Using Drift Compensation

Denis Demchev, *Member, IEEE*, Leif E.B. Eriksson, *Member, IEEE*, Anders Hildeman, and Wolfgang Dierking

***Abstract*—In this article, we investigate the feasibility to align synthetic aperture radar (SAR) imagery based on a compensation for sea ice drift occurring between temporally shifted image acquisitions. The image alignment is a requirement for improving sea ice classification by combining multifrequency SAR images acquired at different times. Images obtained at different radar frequencies provide complementary information, thus reducing ambiguities in the separation of ice types and the retrieval of sea ice parameters. For the alignment we use ice displacement vectors obtained from a sea ice drift retrieval algorithm based on pattern matching. The displacement vectors are organized on a triangular mesh and used for a piecewise affine transformation of the slave image onto the master image. In our case study, we developed an alignment framework for pairs of Advanced Land Observing Satellite-2 PALSAR-2 (L-band) and Sentinel-1 (C-band) images. We demonstrate several successful examples of alignment for time gaps ranging from a few hours to several days, depending on the ice conditions. The data were acquired over three test sites in the Arctic: 1) Belgica Bank, 2) Fram Strait, and 3) Lincoln Sea. We assess the quality of the alignment using the structural similarity index. From the displacement vectors, locations and extensions of patches of strong ice deformation are determined, which allows to estimate the possible areal size of successful alignment over undeformed ice and a judgment of the expected quality for each image pair. The comprehensive assessment of hundreds of aligned L–C SAR pairs shows the potential of our method to work under various environmental conditions provided that the ice drift can be estimated reliably.**

***Index Terms*—Advanced land observing satellite-2 (ALOS-2), alignment, arctic, drift, multifrequency, registration, sea ice, sentinel-1.**

Manuscript received 30 March 2023; revised 30 June 2023 and 31 July 2023; accepted 2 August 2023. Date of publication 7 August 2023; date of current version 14 August 2023. This work was supported in part by the European Space Agency through ESA contract 4000130509/20/NL/FF/ab and in part by "Synergistic Use of L- and C-band SAR Satellites for Sea Ice Monitoring." *(Corresponding author: Denis Demchev.)*

Denis Demchev and Leif E.B. Eriksson are with the Department of Space, Earth and Environment, Division of Geoscience and Remote Sensing of Chalmers University of Technology, SE-412 96 Gothenburg, Sweden (e-mail: denis.demchev@chalmers.se; leif.eriksson@chalmers.se).

Anders Hildeman was with the Chalmers University of Technology, SE-412 96 Gothenburg, Sweden. He is now with the AstraZeneca AB R&D, 431 50 Gothenburg, Sweden (e-mail: hildeman@chalmers.se).

Wolfgang Dierking is with the UiT The Arctic University of Norway, 9019 Tromso, Norway, and also with the Alfred Wegener Institute Helmholtz Centre for Polar and Marine Research, 27570 Bremerhaven, Germany (e-mail: wolfgang.dierking@awi.de).

Digital Object Identifier 10.1109/JSTARS.2023.3302576

I. Introduction

SYNTHETIC aperture radar (SAR) has been used for monitoring and observing sea ice since the 1990s when the ERS-1, ERS-2, and the Radarsat satellites made C-band SAR images available for several regions with seasonal or permanent sea ice cover. SAR acquisitions at C-band have continued and are nowadays complemented by acquisitions at L- and X-band. However, to date L- and X-band data have not been used routinely for operational ice charting because of limitations in spatial coverage and frequency of acquisitions. From early multifrequency airborne SAR data (e.g., [29]) it is known that the combination of different radar bands is of advantage for sea ice mapping. While radar acquisitions at different frequencies can be carried out simultaneously from an airplane, the satellites used for sea ice monitoring carry only single-frequency SAR systems. Due to the continuous movements of large areas of sea ice, multifrequency classification methods that are commonly applied for land areas can only be used for drifting sea ice after images from different SAR sensors, with a temporal gap between their acquisitions, have been aligned or coregistered (registration is the process of making one image conform to another image). In most regions, sea ice drift and deformation are large enough that even if two images are acquired within a few hours, classification algorithms will not be able to take advantage of information from both images without prior correction for local drift and masking of deformed areas. A number of algorithms for drift retrieval have been developed based on feature tracking and/or correlation measures [2], [19], [20]. Future missions may allow for more systematic combinations of different frequencies for sea ice charting (e.g., by ESA's planned ROSE-L mission as complement to Sentinel-1). The potential of methods developed for alignment of multifrequency images over moving targets is one issue which is considered in the planning phase of the ROSE-L/Sentinel-1 data acquisition scenario. In this article, we introduce a framework for the alignment of sea ice images and the assessment of its quality. We use C- and L-band images from three regions in the Arctic with different sea ice conditions, acquired at different seasons and under varying weather conditions. We provide a comprehensive analysis of the benefits and limitations of our method. This study was carried out as part of a project for the European Space Agency (ESA) named: "Synergistic Use of L- and C-Band SAR Satellites for Sea Ice Monitoring," which was led by The Arctic University of Norway in Tromsø.

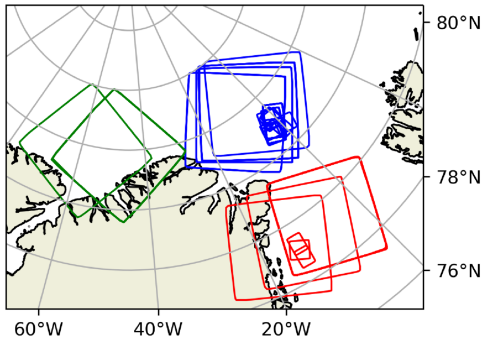

Fig. 1. ALOS-2 image coverage of the three test sites: Green - North Greenland (Lincoln Sea); Blue: Northern Fram Strait region; Red - Belgica Bank.

II. Data and Test Sites

To examine our alignment method we collected L-band advanced land observing satellite-2 (ALOS-2) images at HH polarization from the Greenland and Lincoln Seas, and then collocated them with overlapping C-band Sentinel-1 images at HH polarization. Three regions were chosen as test sites: Belgica Bank, Fram Strait, and North Greenland (Lincoln Sea). The spatial coverage of the collected ALOS-2 scenes for each test site is drawn in Fig. 1. Overlapping Sentinel-1 images are not shown here for clarity. The test sites differ by regional ice dynamics, dominant ice types, and seasonal variations. Hence, we can evaluate the performance of our alignment methodology under a wide range of ice conditions.

A. Test Sites

The Belgica Bank (red squares in Fig. 1) is characterized by an extensive landfast ice area for most of the year, aided by the shallow waters of the Belgica Bank and numerous grounded icebergs that restrict sea ice drift. The sea ice cover in the area is composed of ice that has been advected in from the Fram Strait and ice which has formed locally. As such the sea ice is present in all different stages of development. The interaction between the fast ice area and drift ice causes the development of dynamic ice features including flaw leads, polynyas, and ridging zones [16].

The northern Fram Strait area, blue squares in Fig. 1, is the primary gateway for sea ice moving out of the Arctic Ocean on the Transpolar Drift. The area is characterized by a strong southward drift [30]. This creates a challenge for the alignment of multifrequency images if their acquisitions are not closely synchronized. The ice in this region can be a mixture of all different stages of development. New ice is often present in leads [25]. Further information about typical ice conditions can be found, e.g., in [31].

The Lincoln Sea (North Greenland area), marked by green squares in Fig. 1, is primarily characterized by large floes of multiyear sea ice, often deformed and consolidated and mixed with first-year sea ice. With the reduction in multiyear sea ice in the Arctic, and transition to a more seasonal ice cover [21], the Lincoln Sea is the area forecasted to be the one where multiyear sea ice survives the longest. Sea ice in this area is typically many years old, and heavily ridged. Mostly, the drift is from west to east. If the Nares Strait between Greenland and the Ellesmere Island to the south is open then there is a potential for southward drift [4], [26].

TABLE I
Number of Processed L-C Image Pairs Generated From Sentinel-1 and ALOS-2 Data

Site / mode	Belgica Bank	Fram Strait	North Greenland	Total
FB	9	65	-	74
WB	52	38	65	155
All	61	103	65	251

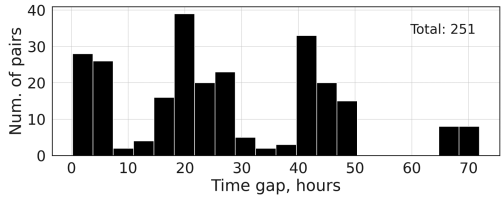

Fig. 2. Distribution of time gaps between image acquisitions for processed L–C image pairs at the test sites.

B. SAR Sea Ice Imagery

Over the three test sites, we collected Level-1.5 ground range detected (GRD) data from ALOS-2 and Level-1 data from Sentinel-1 A/B (the Copernicus Programme satellite constellation) for different months which cover winter, melting, and freezing seasons in the period from April 2019 to February 2020. Two different ALOS-2 data modes are used: 1) ScanSAR nominal and 2) Stripmap Fine. The extra wide swath mode (EW) mode is used for Sentinel-1 data. For both sensors, the backscattering coefficient σ^0 was computed consistently from the digital number DN provided in the datasets as

$$\sigma^0 = DN^2/A^2 \tag{1}$$

where A is a calibration constant from a look-up table found in auxiliary calibration files (for details see [27] and [28]). Then σ^0 is conventionally converted to dB: $\sigma^0_{db} = 10 \cdot \log(\sigma^0)$ and, finally, the data are projected onto a polar stereographic grid with a pixel size of 100 m.

L–C pairs were generated from the images based on the following criteria: The time gap between acquisitions is in the range of 1–72 h (which is determined from the available image pairs); the fraction of the overlap region between the two image must exceed 0.34 (chosen empirically) of the smallest image. In each pair the L- and C-band, images were cropped to the common overlapping area. The final dataset comprises 251 L–C image pairs. The numbers of generated L–C image pairs for each ALOS-2 mode and test site are given in Table I. A histogram of the time gap distribution is shown in Fig. 2.

Site / mode & Belgica Bank & Fram Strait & North Greenland & Total

The incidence angle affects the recognition of ice structures in radar images and the contrast between ice types and ice and water. However, for the success of the alignment of two images, these issues play a minor role compared to the effects of the ice

drift and deformation, spatial resolution, and speckle, and were therefore not considered in our study.

C. Ice Drift and Deformation Data

To obtain sea ice displacements between SAR image pairs, an adapted version of the Chalmers SAR ice drift algorithm [2] was used. The algorithm operates with pattern matching at different processing levels with varying template size and overlap, as well as different stages of down-sampling of the original pixel size. The algorithm also considers rotation of the ice within a template at the highest spatial resolution of the drift field, if the correlation is poor. This is achieved by using the Fourier–Mellin transform. It is assumed that the signature variations of a template in the slave image correspond to a translated and rotated replica of the corresponding template in the master image. In case of larger templates, single local variations of ice floe rotations within the template are not resolved.

For robust drift retrieval, distinct and stable spatial radar intensity variations (caused, e.g., by the presence of leads, ridges, and ice floe edges) visible in both images are required. This means that if an ice structure not present in image 1 occurs in image 2 (i.e., a deformation feature developing between acquisitions of image 1 and image 2) or a structure visible in image 1 cannot be found in image 2 (also due to deformation, e.g., closing of a lead), the matching process is disturbed. Without deformation processes, the ice cover structure remains temporally stable, and the alignment of two SAR images acquired with a time gap of δT is carried out by considering the (deformation-free) drift field. However, even in case of stable ice conditions, it has to be considered that certain ice features or structures may be clearly visible at one frequency but less distinct or not at all at the other. This reduces the magnitude of correlation in pattern matching. Compared to the effect of deformation, the differences between frequencies are a less critical problem.

For this drift algorithm as well as for other state-of-the art drift algorithms ([19], [20]), the problem of judging the accuracy of the retrieved drift vectors needs to be resolved. In order to discard erroneous vectors, we applied the criteria on local vector homogeneity analogously to [5]. The computational grid of the drift algorithm was set to a cell size of 50 $\times$ 50 pixels, corresponding to about 5000 m on the ground. It should be noted that, in our implementation, the chosen drift algorithm can easily be replaced with another algorithm or external drift data if preferred.

The velocity field is used to generate second-order products, such as deformation rates, divergence, and shear. We derive them analogously to [22] from the strain rate tensor. A regular grid has been chosen as, in most cases, it is less affected by errors which arise from boundary definition schemes [10]. For our analysis of the alignment quality in Section IV-B, we calculated ice divergence D and shear S. The calculated values are normalized to a temporal unit of 1 h.

D. Air Temperature At 2 m

The satellite data cover different weather conditions including winter season, freez-up, and melt season. To determine the air temperature over the test sites we used the state-of-the-art atmospheric reanalysis dataset ERA5 [12], which is a part of the Copernicus Climate Change Service (C3S) and is based on the Integrated Forecasting System (IFS) Cy41r2. It has enhanced horizontal resolution of 31 km for various atmospheric parameters with an hourly global coverage. We used the air temperature data at 2-m above ground as an approximation for the temperature at the snow or ice surface. The data were extracted for the period between image acquisitions for each L–C image pair. The temperatures closest in time to the SAR acquisitions were stored together with the maximum and the mean temperature during the period. A mean temperature close to zero degree indicates possible changes between melting and freezing. Maximum temperatures well above zero point to the intensity of a melting episode. Melting of ice or snow between acquisitions can lead to changes in the radar signature. The distribution of the mean air temperatures for the image pairs is shown in Fig. 3 and the maximum values are presented in Fig. 4.

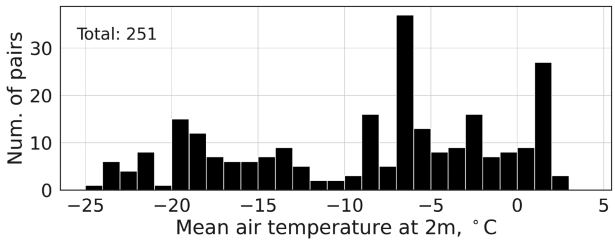

Fig. 3. Mean air temperature at 2 m from ERA5 over test sites between sequential image acquisitions.

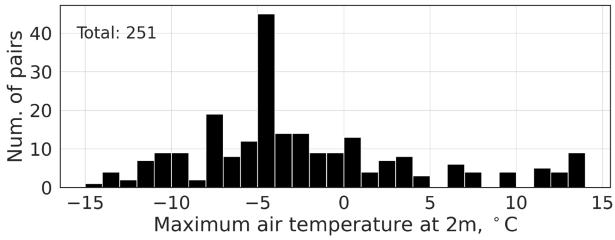

Fig. 4. Maximum air temperature at 2 m from ERA5 over test sites between sequential image acquisitions.

Figs. 3 and 4 reveal that the generated image pairs cover a wide temperature range with mean temperature from −25 °C to +3°C and maximum temperature from −18 °C to +17 °C. This allows the assessment of the alignment performance under a variety of temperature conditions.

III. Alignment Algorithm

The proposed alignment method comprises two main steps: 1) computation of the alignment transformations from estimated ice displacement vectors and 2) execution of the alignment (warping) using the computed alignment transforms. The general scheme of the alignment framework is shown in Fig. 5.

In this study, we use the ALOS-2 images as the master, but both L- and C-band SAR images can be used as master. The ice drift retrieval algorithm yields an output of matching locations

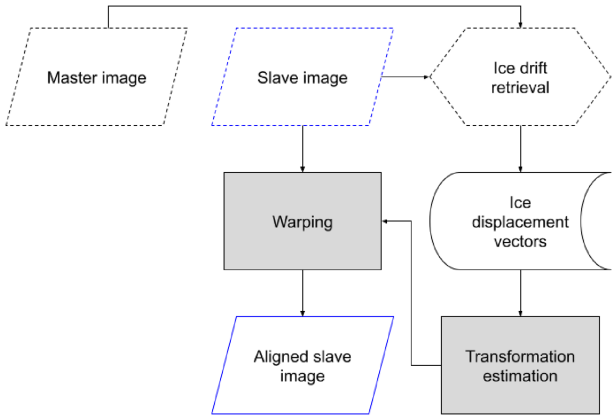

Fig. 5. Workflow for aligning a slave image to a master image.

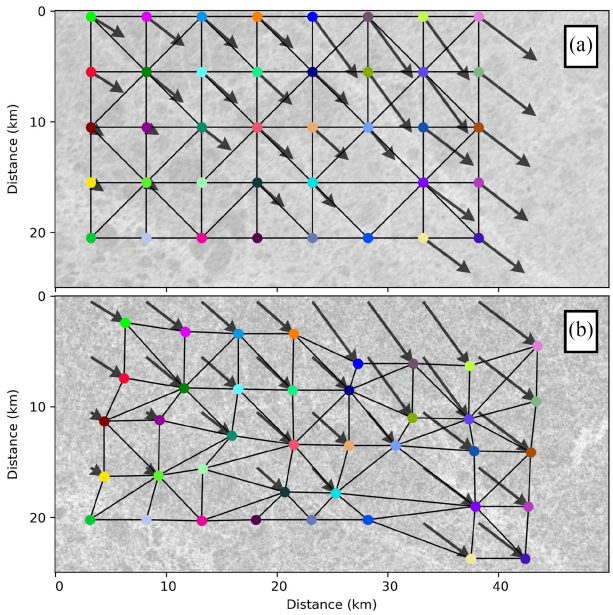

Fig. 6. Triangulation on (a) the master ALOS-2 and (b) slave Sentinel-1 images from the start and end points of the ice displacement vectors. Every color represents a corresponding pair of points.

given by the coordinates in the master image and corresponding coordinates in the slave image. An ice drift vector is determined from the difference in the coordinates of such a pair, denoting the straight-line displacement of the ice between the image acquisitions (the actual pattern of the ice movement can be more complex). A geometric transformation is estimated from the drift data which moves a pixel at coordinates (x, y) to a new position, $(\acute{x}, \acute{y})$. The movement is specified by a pair of transformation equations as follows:

$$\acute{x} = T_x(x, y);\ \acute{y} = T_y(x, y). \tag{2}$$

The alignment problem is to find the appropriate geometric transformation. In our method, we estimate the transformation based on the pairs of points in the master and slave image (a point in the master image marks the start of the drift vector, and the corresponding point in the slave image marks the end, see Fig. 6).

Algorithm 1: Sea Ice SAR Imagery Alignment by Ice Drift Compensation.

Define regular grid over master image as the set of points $\{\mathbf{p_i^m}\}_{\mathbf{i=1}}^{\mathbf{N}}$.
Identify points in slave image corresponding to $\{\mathbf{p_i^m}\}_{\mathbf{i=1}}^{\mathbf{N}}$ as $\{\mathbf{p_i^s}\}_{\mathbf{i=1}}^{\mathbf{N}}$.
Assess quality of each point pair, $\{(\mathbf{p_i^m}, \mathbf{p_i^s})\}_{\mathbf{i=1}}^{\mathbf{N}}$, by local homogeneity criteria. Filter out low quality point pairs, i.e., the set of remaining point pair indices includes R elements.
Triangulate the region of the master image into a triangular mesh, T^m. The nodes of this mesh are the points $\{\mathbf{p_i^m}\}_{\mathbf{i}\in\mathbf{R}}$. Likewise, the triangular mesh T^s has the corresponding nodes $\{\mathbf{p_i^s}\}_{\mathbf{i}\in\mathbf{R}}$.
for $t^m, t^s \in (T^m, T^s)$ **do**
  Compute affine spatial transformation between t^m and t^s, i.e., the current triangle in the master image and the corresponding triangle in the slave image. Also, compute the corresponding transform between t^s and t^m, i.e., the inverse transform.
end
for $t^m, t^s \in (T^m, T^s)$ **do**
  Warp the pixels of the slave image inside t^s onto the t^m using the inverse transform, or use the forward transform if you want to map the master image onto the slave.
end

Due to the brittle nature of sea ice and the deformation it undergoes, the number of drift vectors will often be limited. Therefore, due to robustness issues and limited information we approximate the actual geometric transformation with a piecewise affine transformation [9]. If 2-D points are represented in vector form, an affine transformation consists of multiplication by a 2×2 matrix followed by the addition of a vector:

$$\begin{bmatrix} \acute{x} \\ \acute{y} \end{bmatrix} = \begin{bmatrix} a_0 & a_1 \\ b_0 & b_1 \end{bmatrix} \begin{bmatrix} x \\ y \end{bmatrix} + \begin{bmatrix} a_2 \\ b_2 \end{bmatrix}. \tag{3}$$

We apply the affine transformation in the triangular region between three neighboring points. An example of triangulation based on ice displacement vectors for an image pair is shown in Fig. 6, where every color corresponds to a certain displacement vector.

In this work, we implemented the piecewise affine transformation using a scikit-image's function [18]. The core idea is to use a number of local mapping functions, each tuned to map well in local neighborhoods. Then by piecing the local mapping functions together, a global mapping function is obtained. Based on this principle, we developed an alignment framework written in Python [13]. A description of the framework stages is given in the pseudocode in Algorithm 1.

IV. Results and Discussion

In this section, we present the results of the evaluation of the alignment method proposed in [7] based on 251 L–C image pairs obtained under various ice and weather conditions, and time differences between image acquisitions. Sea ice displacement

vectors are derived at every 50 pixels over the overlapped areas with the SAR drift algorithm [2].

A. Alignment Feasibility

In first analyses presented in [7], we showed examples of alignment for image pairs acquired with a time difference of up to 32 h, and concluded that the alignment is possible for the pairs that are acquired with larger time gaps but over only slowly changing ice conditions. Here, we extended our analyses and found an example for which the alignment was even possible between images acquired with a 72-h temporal gap. The original and aligned ALOS-2 image and the ice displacement field are shown in Fig. 7. The drift vectors were obtained evenly for all computational grid cells which resulted in the successful alignment of the slave L-band image to the master C-band image without visible distortion. In general, the correctness of alignment (minimized image distortion) depends on the accuracy and spatial distribution of the drift vectors.

As ice motion is complex and heterogeneous in many cases, it is difficult to provide general recommendations regarding the sufficient number and spatial distribution of drift vectors for successful alignment. For instance, only a few correct drift vectors might be sufficient for the alignment in the case of homogeneous ice drift, while heterogeneous ice motion requires more detailed drift data at higher spatial density. Hence, the drift field should be retrieved from the smallest meaningful grid cells. The size of the latter must cover a sufficient number of pixels to clearly identify structures and texture which influence the uncertainty of the correlation in the process of pattern matching.

In our alignment framework, we follow the strategy of extracting evenly distributed matching points on regular grids, which was used in several studies [1], [17], [24]. However, as mentioned above, the limitation of this strategy with its fixed grid cell sizes is that regional variations of the sea ice cover structure cannot be considered directly during pattern matching. In [11], the authors proposed an objective function that considers the precision of the matching points and their distribution including triangle shapes to optimize the number of correspondences that are used for satellite image coregistration. Despite this optimization step being out of the scope of this study, it can be a part of future work for the improvement of our alignment method.

B. Texture Similarity Measure in Aligned Images

For an objective assessment of the alignment quality to be expected or achieved, different metrics are available. In the first case, the image pair can be analyzed with regard to similarities of intensity (brightness) variations before carrying out the alignment; in the latter case, the correctness of the alignment is judged.

For our application, we found that the structural similarity index (SSIM) [32] is the most appropriate metrics to measure the similarity between two images in terms of intensity, contrast, and structure

$$\mathrm{SSIM}(x,y) = f(I(x,y), c(x,y), s(x,y))$$

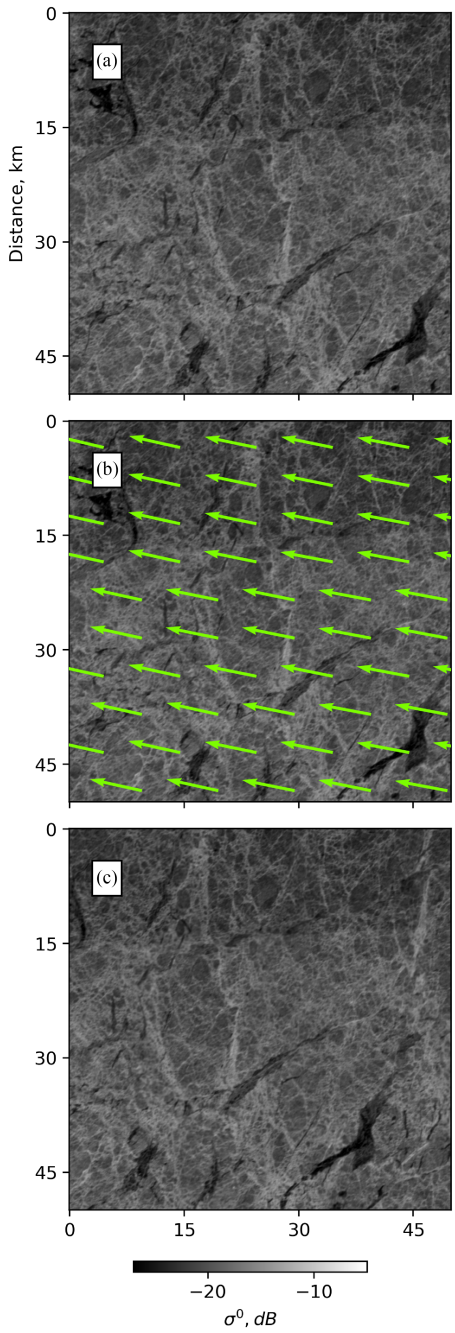

Fig. 7. (a) ALOS-2 ScanSAR image from 2019-10-28 17:40:22; (b) Magnitude and direction of the drift vectors (green) that are derived in the common area between 2019-10-28 17:40:22 (ALOS-2) and 2019-10-31 17:00:40 (Sentinel-1). Drift vectors are displayed for every 50 pixels (5 km); (c) Aligned ALOS-2 image by the ice drift compensation.

$$I(x,y) = \frac{2\mu_x\mu_y + C_1}{\mu_x^2 + \mu_y^2 + C_1}$$
$$c(x,y) = \frac{2\sigma_x\sigma_y + C_2}{\sigma_x^2 + \sigma_y^2 + C_2}$$
$$s(x,y) = \frac{\sigma_{xy} + C_3}{\sigma_x\sigma_y + C3} \tag{4}$$

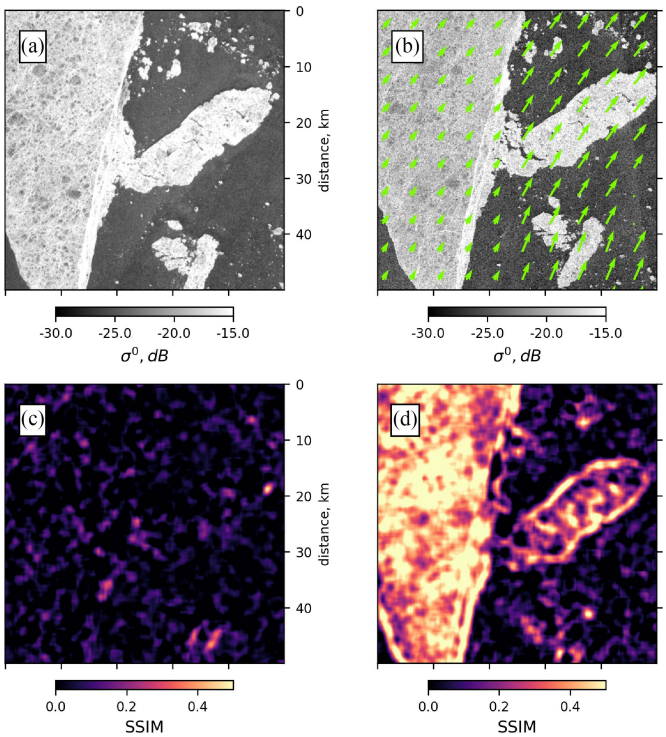

Fig. 8. L–C sea ice imagery pair alignment in the marginal ice zone and quality assessment using the SSIM index. (a) L-band ALOS-2 image; (b) C-band Sentinel-1 image with the ice displacement vectors on top; (c) SSIM before the alignment; (d) SSIM after the alignment.

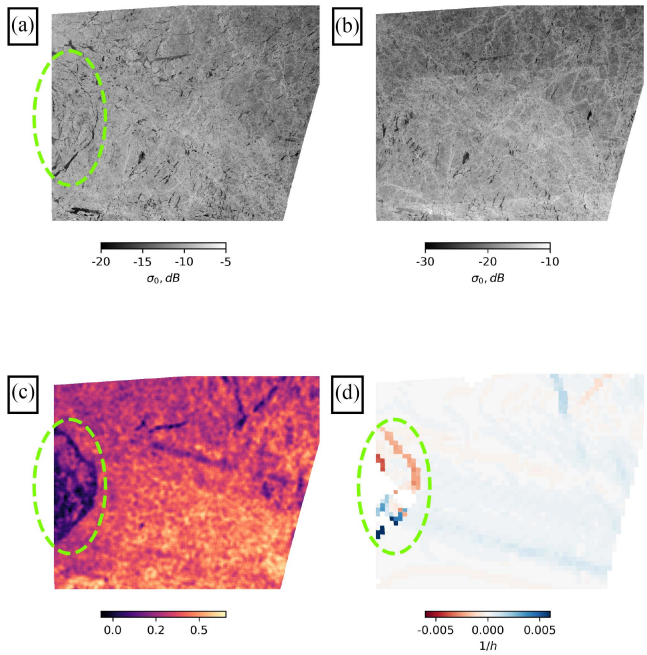

Fig. 9. (a) Aligned Sentinel-1 image from 27 November 2019, 19:03:40 UTC. (b) The master ALOS-2 image from 25 November 2019, 17:41:15 UTC. (c) SSIM. (d) Ice divergence rate. A zone of intense deformation outlined with green dashed line.

where I is intensity, c is contrast, s is structure, μ is mean, σ is variance, and σ_{xy} is covariance. $C1, C2, C3$ are the stabilization constants. The SSIM takes values between 0 (no similarity) to 1 (perfect match). For details see [32].

The advantage of the SSIM is that it uses the structural information in an image independent of the average intensity. This is an important aspect in the alignment of radar images acquired at different frequencies, polarizations, and incidence angles, since they reveal different levels of intensity and contrasts between different ice types, between ice and water, as well as between level and deformed ice. It should be noted that, due to these differences, we cannot expect the SSIM values being close to 1 even in ideal alignment cases if the images differ in frequency, polarization, and incidence angle.

To demonstrate the applicability of the SSIM, an example of aligned images in the Fram Strait is shown in Fig. 8. Here, the SSIM values are significantly larger after the alignment (D) than before the alignment (C). For instance, after the alignment, the two large floes can be recognized by SSIM values above 0.4, which is a positive indication of successful alignment.

Another example of applying the SSIM metrics for the L–C image alignment assessment is provided for a pair of Sentinel-1 and ALOS-2 images from North Greenland (Lincoln Sea 83.405 N 55.543 W) in Fig. 9. The images were taken with a time difference of 48 h, and the SSIM is shown together with ice divergence and shear rate. The quality metrics have been calculated for a window size of 50 × 50 for each pixel, which corresponds to the grid cell size used for drift and deformation retrieval. As the magnitudes of divergence and shear in Fig. 9 reveal, the strongest ice deformation occurred in an area on the left side of the images (outlined with a green dashed line in the Sentinel-1 image). Because of the deformation, the ice structures in this area are different between the ALOS-2 and Sentinel-1 images, and a successful alignment cannot be expected there.

The SSIM provides useful information on the similarity of ice features between the L- and C-band image. The zones of high values (0.4–0.6) correspond to structures found in both images (successful alignment) and zones of low values and match well with the changes of the ice structure due to deformation between the acquisitions of the two images. This example confirms that the SSIM metric is invariant to absolute intensity, which is particularly beneficial for multifrequency image analysis, where inherent signature differences between the different bands significantly complicate an objective quality assessment.

C. *Thresholds Separating Weak and Strong Deformation*

Ice deformation is a limiting factor for alignment as it causes changes of ice structures between image 1 and image 2 (e.g., closing of a lead). Thus, the knowledge of local deformation rates can be useful to assess the potential for a successful match of the C- and L-band image before carrying out the alignment. The basic idea here is to define deformation magnitude thresholds and use them to separate areas that can easily be aligned from those for which deformation is too heavy.

The threshold values of deformation parameters are determined on the grid of the drift vectors. The grid cells are of square shape, contain several pixels and usually also show recognizable ice structures. According to [6], the geolocation

error of Sentinel-1 images is much smaller than a single pixel. Hence it is assumed that the tracking error is dominant and terms dependent on the geolocation uncertainties are neglected. The deformation uncertainty is calculated from (for details see [6])

$$\sigma_{\text{tot}}^2 = \sigma_{\text{div}}^2 = \sigma_{\text{shr}}^2 = \frac{2\sigma_{tr}^2}{\Delta T^2\, L^2} \tag{5}$$

where σ is the error variances for the total deformation (σ_{tot}), divergence (σ_{div}), and shear (σ_{shear}) rates; σ_{tr} is the ice tracking uncertainty; ΔT is the time interval between the two SAR images from which drift/deformation is evaluated; L is the side length of a square grid cell which is set to 50 pixels in our case. With a tracking error of $b\Delta p$ (where b is a real number and Δp is pixel size)

$$\sigma_{\text{tot}}^2 = \frac{2b^2\Delta p^2}{\Delta T^2\, L^2}. \tag{6}$$

For the calculations of thresholds, the following numbers are valid: the ice tracking error is one pixel, hence $b = 1$ in (6); the grid size for calculating the drift is $L = 5$ km, and the pixel size 100 m. We consider magnitudes of total deformation that are larger than the uncertainty calculated from (6) as real deformation. The time gaps between images of single pairs from the test sites are provided as a histogram in Fig. 2. With the numbers for b, Δp, and L give above, the uncertainty for a time gap of, e.g., 24 h is 0.001 h^{-1}, and using the time gaps in Fig. 2 it is $0.028/\Delta T$.

D. Alignment Quality Assessment

For a comprehensive quality assessment of alignment, we chose a combination of derived local SSIMs and fractions of deformed ice. The advantage of this approach is that it allows to complement ice deformation-related information (the temporal component) with texture similarity (spatial component) between the master and slave SAR images. To give an impression of how the two metrics complement each other, let us consider an example of alignment quality assessment for an L–C pair obtained over North Greenland (Lincoln Sea) in November 2019 shown in Fig. 10.

From Fig. 10, it is obvious that areas of stronger total deformation match areas with lower SSIM values. In the areas with a lack of ice deformation data (due to gaps in the field of ice drift vectors), the SSIM metric still provides alignment quality information over the distorted area in the dashed white circle. In some parts of the image, the total deformation is relatively low but above the threshold (time gap between acquisitions around 43 h, temporal threshold < 0.0007), and the SSIM indicates very low correspondence between master and slave (in yellowish). Ice deformation can therefore be used as a first-guess estimation of alignment success as it reveals how much ice has undergone a not negligible deformation that might result in texture distortion. It can easily be computed from ice drift data and does not require much computation effort while the SSMI provides a more detailed picture as it is computed for every image pixel. At the same time, they both complement each other and give a more comprehensive assessment of alignment quality.

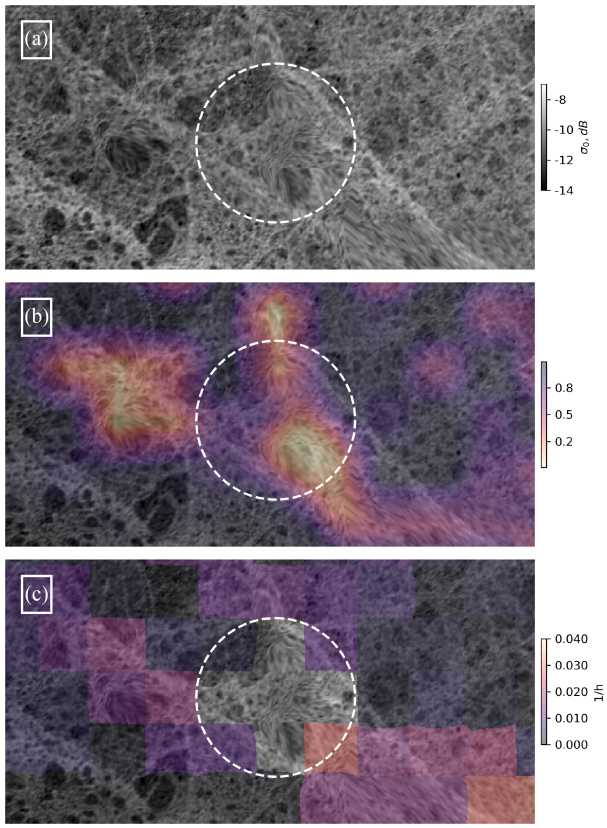

Fig. 10. (a) Aligned ALOS-2 SAR image acquired at 2019/09/02 at 17:40:21 UTC. (b) SSIM metric. (c) Total ice deformation rate. The zones with high ice deformation values correspond well with low values of SSIM. White dashed circle indicates a lack of deformation data.

E. Alignment Quality Under Different Ice and Weather Conditions

Since L- and C-band image acquisitions from presently operational satellite missions are only possible with temporal gaps between them, it is of interest to assess the alignment quality of a larger number of L–C image pairs acquired for different conditions. To this end, we processed 251 L–C image pairs over three test sites: 1) Belgica Bank, 2) Fram Strait, and 3) Lincoln Sea, which are characterized by different ice drift regimes and environmental conditions in the period April 2019 to February 2020. The results are summarized in three plots in Fig. 11.

From Fig. 11, several observations can be made. The probability of a large texture structure similarity (SSIM) is slightly higher when the time gap between the SAR image acquisitions is shorter [Fig. 11(a)]. However, several SSIM values obtained at larger time differences are higher than for smaller temporal gaps which is due to the large influence of the local ice drift and deformation magnitude. A decreasing tendency for SSIM associated with warmer weather conditions can be recognized from Fig. 11(b). This is in agreement with the fact that under melting condition, ice types are more difficult to separate, and ice structures caused, e.g., by clusters of ridges are more difficult to identify.

In Fig. 11(c), the SSIM texture similarity metric is shown versus the deformed ice fraction. The fraction of deformed ice is

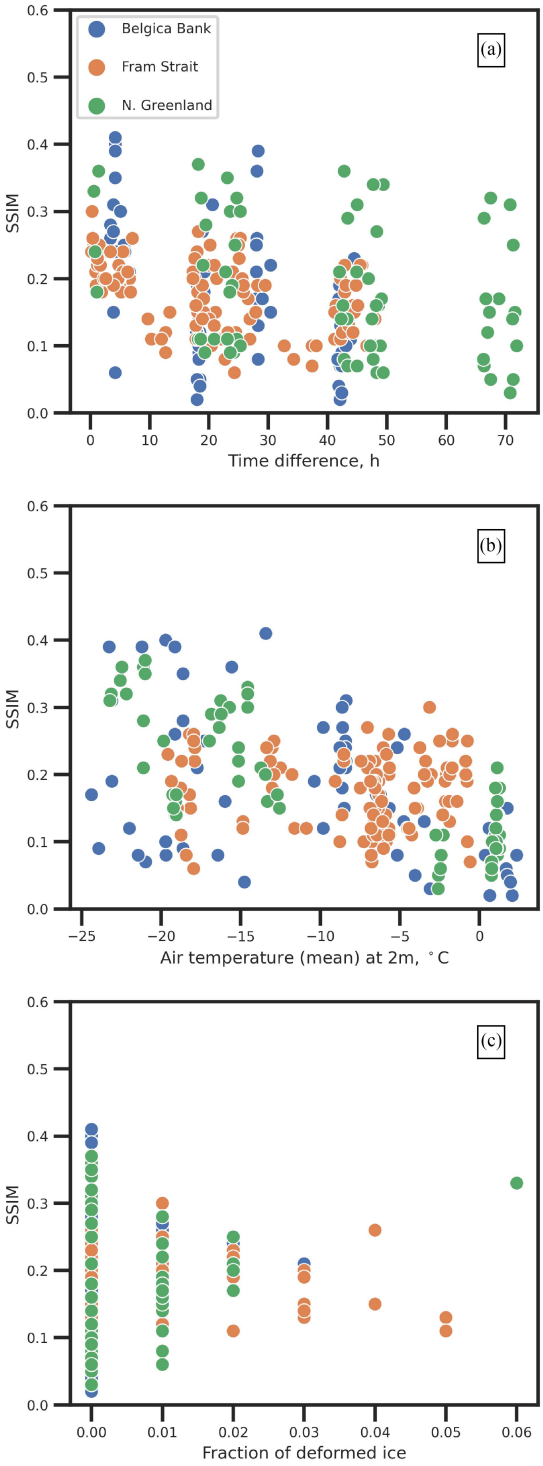

Fig. 11. (a) SSIM against temporal gap between acquisitions. (b) SSIM against mean air temperature at 2 m. (c) SSIM against areal fraction of deformed ice. The values have been obtained for 251 L–C SAR image pairs.

given relative to the area of successful drift vector retrievals. We observe that a wide range of SSIM values can be associated with different levels of ice deformation, but the number of relatively strong structural texture similarity tends to correspond to the lower fraction of deformed ice. This observation is expected as the ice deformation reduces the possibility to identify the ice feature in sequential images even when acquired at a single frequency. However, a low deformation rate will not always lead to a high SSIM, because the latter judges contrast and structure besides intensity. Since the difference of radar signatures between L- and C-band varies depending on local ice conditions, the SSIM may be low even if no ice deformation takes place.

The prevailing deformed ice fraction for the processed L–C image pairs is in the range of 0–10%. The relatively high values of SSIM that characterize structural SAR texture similarity are associated with lower deformed ice fraction and colder air temperature over the ice surface. Overall, we obtained mostly relatively low magnitudes < 0.25 of the SSIM. Visual inspection of the images showed that sometimes smaller patches of considerable distortions, as shown in Fig. 10, occurred which are due to strongly localized ice deformation, while large parts of the overlap area could successfully be aligned. However, occasionally, alignment was not possible over larger parts of the overlap area but only over a smaller fraction of it. From our results, it is important to notice that the temporal gap between L- and C-band image acquisitions is not a sufficient stand-alone criterion for the expected success of alignment, the characteristics of the local ice drift regime and seasonal effects, such as melting have to be taken into account as well [3], [15]. It has also to be considered that we did not include image pairs from the sites of highly mobile sea ice regimes, such as the marginal ice zone, or around the southern tip of Greenland and along the eastern Labrador coast, since the reliability of the retrieved drift fields, if a retrieval is possible at all, can be expected to be very low based on our experience [14], [23].

V. Conclusion

In this study, we investigated the potential of multifrequency sea ice SAR imagery alignment by ice drift compensation for pairs of L- (ALOS-2) and C-band (Sentinel-1) satellite SAR images. An alignment framework has been developed and its performance was evaluated using SAR images acquired with a time separation from a few to 72 h over test sites in the Arctic region: Belgica Bank, Fram Strait, and North Greenland (Lincoln Sea), which are characterized by the presence of different ice types (multiyear, first-year, young, and new ice) and cover the marginal ice zone and various ice dynamics regimes. The core of the framework is based on a piecewise affine transform that utilize geometrical information from ice displacement vectors in order to align two sequential images. The alignment is performed using local transformations obtained for triangular areas, which map any point in one image to its appropriate position in the second image. The transformation accounts for pure rotation, translation, and includes stretching.

The conditions under which the alignment is possible were defined as important feedback to the design of future SAR missions operated as satellite constellations. To answer the question whether alignment is possible for multifrequency analysis, and under which conditions it works, we developed and validated procedures for matching of C- and L-band image data acquired at different times, and quantified the performance in the alignment of these data. We assessed the impact of temporal intervals

between consecutive C- and L-band image acquisitions, considering the degree of ice deformation and the effect of surface air temperatures, the latter for judging the effect of premelting and melting conditions. For the alignment quality assessment, we proposed the combined use of two kinds of metrics: 1) fraction of deformed ice [8] and 2) texture similarity metric (SSIM) [32]. The fraction of deformed ice relies on predefined ice deformation rate thresholds to detect areas covered by deformed ice and is used as a proxy for a possible amount of distortions caused by deformation processes between image acquisitions. The structural similarity measure (SSIM) compares local differences between two images considering normalized intensity, contrast, and covariance, and is used for judging the success of alignment over the overlapping region in the image. We showed that the feasibility of the alignment mainly depends on the following factors: Number and density of correct ice drift vectors, degree of ice deformation, and weather conditions that lead to surface melting or other changes which result in weaker signature contrast between different ice areas and structures.

Our suggested methodology is a promising step for joint analyses of multifrequency SAR imagery of sea ice acquired at different times, which can be extended also to other frequencies than C- and L-band.

Acknowledgment

The authors would like to thank Johannes Philipp Lohse for the calibration program code for ALOS-2 data, and Malin Johansson for proofreading and valuable discussions which greatly helped to get this work done. Both are from the Centre for Integrated Remote Sensing and Forecasting for Arctic Operations, UiT The Arctic University of Norway, Tromsø, Norway. ALOS-2/PALSAR-2 data are provided by JAXA through the 2019 to 2022 mutual cooperation project between ESA and JAXA on Using Synthetic Aperture Radar Satellites in Earth Science and Applications. Sentinel-1 data were provided free of charge by the European Union Copernicus program and were downloaded from the Alaska Satellite Facility (ASF) SAR Distributed Active Archive Center (DAAC).

Code availability

The Python code for SAR sea ice imagery alignment by ice drift compensation and usage examples are available at [13].

References

[1] V. Arévalo and J. González, "An experimental evaluation of non-rigid registration techniques on QuickBird satellite imagery," *Int. J. Remote Sens.*, vol. 29, no. 2, pp. 513–527, 2008.

[2] A. Berg and L. E. Eriksson, "Investigation of a hybrid algorithm for sea ice drift measurements using synthetic aperture radar images," *IEEE Trans. Geosci. Remote Sens.*, vol. 52, no. 8, pp. 5023–5033, Aug. 2014.

[3] J. A. Casey et al., "Separability of sea ice types from wide swath C- and L-band synthetic aperture radar imagery acquired during the melt season," *Remote Sens. Environ.*, vol. 174, pp. 314–328, 2016.

[4] O. Dyre et al., "Mapping pan-arctic landfast sea ice stability using Sentinel-1 interferometry," *Cryosphere*, vol. 13, no. 2, pp. 557–577, 2019.

[5] D. Demchev, V. Volkov, E. Kazakov, P. F. Alcantarilla, S. Sandven, and V. Khmeleva, "Sea ice drift tracking from sequential SAR images using accelerated-KAZE features," *IEEE Trans. Geosci. Remote Sens.*, vol. 55, no. 9, pp. 5174–5184, Sep. 2017.

[6] W. Dierking, H. L. Stern, and J. K. Hutchings, "Estimating statistical errors in retrievals of ice velocity and deformation parameters from satellite images and buoy arrays," *Cryosphere*, vol. 14, no. 9, pp. 2999–3016, 2020.

[7] L. E. Eriksson, D. Demchev, A. Hildeman, and W. Dierking, "Alignment of L-and C-band SAR images for enhanced observations of sea ice," in *Proc. IEEE Int. Geosci. Remote Sens. Symp.*, 2022, pp. 3798–3801.

[8] A. Gegiuc, M. Similä, J. Karvonen, M. Lensu, M. Mäkynen, and J. Vainio, "Estimation of degree of sea ice ridging based on dual-polarized C-band SAR data," *Cryosphere*, vol. 12, no. 1, pp. 343–364, 2018.

[9] A. Goshtasby, "Piecewise linear mapping functions for image registration," *Pattern Recognit.*, vol. 19, no. 6, pp. 459–466, 1986.

[10] J. Griebel and W. Dierking, "Impact of sea ice drift retrieval errors, discretization and grid type on calculations of ice deformation," *Remote Sens.*, vol. 10, no. 3, 2018, Art. no. 393.

[11] Y. Han, J. Choi, Y. Byun, and Y. Kim, "Parameter optimization for the extraction of matching points between high-resolution multisensor images in urban areas," *IEEE Trans. Geosci. Remote Sens.*, vol. 52, no. 9, pp. 5612–5621, Sep. 2014.

[12] H. Hersbach et al., "The ERA5 global reanalysis," *Quart. J. Roy. Meteorological Soc.*, vol. 146, no. 730, pp. 1999–2049, 2020.

[13] A. F. Hildeman and D. Demchev, "SAR sea ice imagery alignment framework," 2021. Accessed: Jul. 23, 2023. [Online]. Available: https://github.com/xdenisx/ice_drift_pc_ncc/tree/main/tools/align

[14] T. Hollands and W. Dierking, "Performance of a multiscale correlation algorithm for the estimation of sea-ice drift from SAR images: Initial results," *Ann. Glaciology*, vol. 52, no. 57, pp. 311–317, 2011.

[15] S. E. Howell et al., "Comparing L-band C-band synthetic aperture radar estimates of sea ice motion over different ice regimes," *Remote Sens. Environ.*, vol. 204, pp. 380–391, 2018.

[16] N. E. Hughes, J. P. Wilkinson, and P. Wadhams, "Multi-satellite sensor analysis of fast-ice development in the Norske øer Ice Barrier, northeast Greenland," *Ann. Glaciology*, vol. 52, no. 57, pp. 151–160, 2011.

[17] C. Huo, C. Pan, L. Huo, and Z. Zhou, "Multilevel SIFT matching for large-size VHR image registration," *IEEE Geosci. Remote Sens. Lett.*, vol. 9, no. 2, pp. 171–175, Mar. 2012.

[18] Scikit Image: Image Processing in Python, "Piecewise affine transformation function (Python)," 2022. Accessed: Dec. 17, 2022. [Online]. Available: https://github.com/scikit-image/scikit-image/blob/00177e14097237ef20ed3141ed454bc81b308f82/skimage/transform/_geometric.py#L934-L1069

[19] A. S. Komarov and D. G. Barber, "Sea ice motion tracking from sequential dual-polarization RADARSAT-2 images," *IEEE Trans. Geosci. Remote Sens.*, vol. 52, no. 1, pp. 121–136, Jan. 2014.

[20] A. A. Korosov and P. Rampal, "A combination of feature tracking and pattern matching with optimal parametrization for sea ice drift retrieval from SAR data," *Remote Sens.*, vol. 9, no. 3, 2017, Art. no. 258.

[21] R. Kwok, "Arctic sea ice thickness, volume, and multiyear ice coverage: Losses and coupled variability (1958–2018)," *Environmen. Res. Lett.*, vol. 13, no. 10, Oct. 2018, Art. no. 105005.

[22] R. W. Lindsay and H. Stern, "The RADARSAT geophysical processor system: Quality of sea ice trajectory and deformation estimates," *J. Atmospheric Ocean. Technol.*, vol. 20, no. 9, pp. 1333–1347, 2003.

[23] S. Linow, T. Hollands, and W. Dierking, "An assessment of the reliability of sea-ice motion and deformation retrieval using SAR images," *Ann. Glaciology*, vol. 56, no. 69, pp. 229–234, 2015.

[24] D. Liu, P. Gong, M. Kelly, and Q. Guo, "Automatic registration of airborne images with complex local distortion," *Photogrammetric Eng. Remote Sens.*, vol. 72, no. 9, pp. 1049–1059, 2006.

[25] M. Mäkynen and M. Similä, "Thin ice detection in the Barents and Kara Seas using AMSR2 high-frequency radiometer data," *IEEE Trans. Geosci. Remote Sens.*, vol. 57, no. 10, pp. 7418–7437, Oct. 2019.

[26] G. Moore, S. Howell, M. Brady, X. Xu, and K. McNeil, "Anomalous collapses of Nares Strait ice arches leads to enhanced export of Arctic sea ice," *Nature Commun.*, vol. 12, no. 1, 2021, Art. no. 1.

[27] T. Motohka, O. M. I. Sakashita, and M. Shimada, "ALOS-2 PALSAR-2 calibration/validation updates," in *Proc. JAXA/EORC Joint PI Meeting Glob. Environ. Observation Mission FY2017*, 2018, vol. 24, p. 6.

[28] R. Piantanida, G. Hajduch, and J. Poullaouec, "Sentinel-1 Level-1 detailed algorithm definition," ESA, Paris, France, Tech. Rep. SEN-TN-52-7445, 2016.

[29] E. Rignot and M. R. Drinkwater, "Winter sea-ice mapping from multi-parameter synthetic-aperture radar data," *J. Glaciology*, vol. 40, no. 134, pp. 31–45, 1994.

[30] L. H. Smedsrud, M. H. Halvorsen, J. C. Stroeve, R. Zhang, and K. Kloster, "Fram Strait sea ice export variability and Sep. arctic sea ice extent over the last 80 years," *Cryosphere*, vol. 11, no. 1, pp. 65–79, 2017.
[31] P. Wadhams, N. Hughes, and J. Rodrigues, "Arctic sea ice thickness characteristics in winter 2004 and 2007 from submarine sonar transects," *J. Geophysical Res.: Oceans*, vol. 116, no. C8, pp. 3–10, 2011.
[32] Z. Wang, A. C. Bovik, H. R. Sheikh, and E. P. Simoncelli, "Image quality assessment: From error visibility to structural similarity," *IEEE Trans. Image Process.*, vol. 13, no. 4, pp. 600–612, Apr. 2004.

Denis Demchev (Member, IEEE) received the Ph.D. degree in oceanography from Saint-Petersburg State University, St. Petersburg, Russia, in 2019.

He was a leading Programmer with the Center for Ice and Hydrometeorogical Information, Arctic and Antarctic Research Institute, St. Petersburg, Russia, and a Researcher with the Nansen International and Remote Sensing Center, St. Petersburg, Russia, from 2007 to 2019. In 2019, he was a Project Assistant with the Chalmers University of Technology, Gothenburg, Sweden. From 2020 to 2022, he was a Researcher with the Nansen Environmental and Remote Sensing Center, Bergen, Norway. He has participated in several scientific cruises to the Arctic and the Baltic Sea as an Ice Adviser and Analyst. He is currently with the Department of Space, Earth, and Environment, Chalmers University of Technology. His research interests include sea ice dynamics retrieval and validation from satellite SAR data with a particular interest in localization of ice deformation features like ridges and leads.

Leif E.B. Eriksson (Member, IEEE) received the university certificate in space technology from Umeå University, Umeå, Sweden, in 1993, the M.S. degree in electrical engineering from the Chalmers University of Technology, Gothenburg, Sweden, in 1998, and the Ph.D. degree in natural sciences from Friedrich Schiller University, Jena, Germany, in 2004.

From 1999 to 2000, he was with the Space Application Institute, Joint Research Centre of the European Commission, Ispra, Italy. From 2000 to 2004, he was with the Department of Geoinformatics, Friedrich-Schiller University, Jena, Germany. In 2004, he joined the radar remote sensing group with the Chalmers University of Technology. Since 2022, he has been holding a position as Professor of Radar Remote Sensing with the Department of Space, Earth and Environment, Chalmers University of Technology. His research interests include the use of SAR to retrieve information about ocean, sea ice, and forest.

Anders Hildeman received the Ph.D. degree in spatial statistics from the Department of Mathematical Sciences, Chalmers University of Technology, Gothenburg, Sweden, in 2019.

From 2019 to 2021, he was with the Department of Space, Earth, and Environment, Chalmers University of Technology. Since 2021, he has been a Senior Data Scientist with AstraZeneca, Gothenburg, Germany. His research interests include Gaussian processes in space and time and deep learning image analysis.

Wolfgang Dierking received the M.Sc. degree in geophysics from the University of Hamburg, Hamburg, Germany, in 1985, and the Ph.D. degree in physics (ocean remote sensing) from the University of Bremen, Bremen, Germany, in 1989.

Since 2002, he has been with the Helmholtz Centre for Polar and Marine Research, Alfred Wegener Institute (AWI), Bremerhaven, Germany, and since 2016, he has been a Professor II with the Centre for Integrated Remote Sensing and Forecasting for Arctic Operations, UiT The Arctic Univesity of Norway, Tromsø, Norway, where he leads a group working with remote sensing of sea ice and icebergs. From 2007 to 2019, he was the Head of the research group Earth Observation Systems, AWI. The group dealt with remote sensing of sea ice, ice sheets, and permafrost regions. In 2007, he was a Visiting Professor with the Chalmers University of Technology, Gothenburg, Sweden. From 1996 to 2002, he held a position as Associate Research Professor with the Danish Centre for Remote Sensing, Technical University of Denmark, Kongens Lyngby, Denmark. He was a member of different advisory groups of the European Space Agency, Paris, France. Recently, he became a member of the Copernicus L-Band SAR Mission Advisory Group, and, in 2021, a member of the Sentinel-1 Next Generation Mission Advisory Group. He participated in several field expeditions to the Arctic, Antarctic, and the Baltic Sea. His research interests include remote sensing of the polar regions.